

HLGFA: High–Low Resolution Guided Feature Alignment for Unsupervised Anomaly Detection

Han Zhou¹, Yuxuan Gao¹, Yinchao Du¹, and Xuezhe Zheng¹

Innolight Technology Research Institute
{han.zhou, yuxuan.gao, yinchao.du, xuezhe.zheng}@innolight.com

Abstract. Unsupervised industrial anomaly detection (UAD) is essential for modern manufacturing inspection, where defect samples are scarce and reliable detection is required. In this paper, we propose **HLGFA**, a high-low resolution guided feature alignment framework that learns normality by modeling cross-resolution feature consistency between high-resolution and low-resolution representations of normal samples, instead of relying on pixel-level reconstruction. Dual-resolution inputs are processed by a shared frozen backbone to extract multi-level features, and high-resolution representations are decomposed into structure and detail priors to guide the refinement of low-resolution features through conditional modulation and gated residual correction. During inference, anomalies are naturally identified as regions where cross-resolution alignment breaks down. In addition, a noise-aware data augmentation strategy is introduced to suppress nuisance-induced responses commonly observed in industrial environments. Extensive experiments on standard benchmarks demonstrate the effectiveness of HLGFA, achieving **97.9% pixel-level AUROC** and **97.5% image-level AUROC** on the MVTec AD dataset, outperforming representative reconstruction-based and feature-based methods.

Keywords: Unsupervised Anomaly Detection · Feature Alignment · Multi-Resolution Learning

1 Introduction

Industrial anomaly detection (IAD) is a fundamental component of modern manufacturing quality control, aiming to automatically identify defects or irregularities without human intervention. With the rapid deployment of automated production lines, reliable visual inspection systems have become essential across a wide range of industries, where manual inspection is often inefficient, error-prone, and difficult to scale.

Despite substantial progress in computer vision, IAD remains challenging due to several inherent factors: the extreme imbalance between normal and defective samples, the large diversity and unpredictability of defect appearances, and the presence of complex industrial backgrounds that can obscure or mimic defects. Moreover, real-world applications demand high precision and recall, as missed or false detections may lead to significant economic loss or safety risks.

Unsupervised anomaly detection (UAD) has therefore attracted increasing attention, as it learns normal patterns solely from defect-free samples and identifies anomalies as deviations during inference. Existing UAD approaches can be broadly grouped into reconstruction-based methods [20], feature-based methods such as PatchCore [15] and UniAD [18], and more recent zero-shot or few-shot paradigms leveraging vision-language models [5, 8, 9]. While effective, many existing methods struggle to simultaneously preserve global structural consistency and local detail fidelity, especially when defects vary significantly in scale.

A key observation in industrial inspection is that normal patterns exhibit stable feature responses under resolution variation, whereas anomalous regions are considerably more sensitive to resolution reduction. When images are down-sampled, the global structure of normal objects is largely preserved, while defect-related cues—typically local and irregular—tend to degrade or shift. This suggests that cross-resolution feature consistency provides an intrinsic cue for normality, whereas pronounced inconsistencies naturally indicate anomalies. As illustrated in Fig. 1, normal samples maintain consistent responses across resolutions, while anomalous samples exhibit clear response shifts, offering a principled signal for unsupervised anomaly detection without explicit defect modeling.

Motivated by this observation, we propose HLGFA, a high–low resolution guided feature alignment framework for unsupervised industrial anomaly detection. Instead of relying on pixel-level reconstruction, HLGFA models normality by enforcing cross-resolution feature consistency between high-resolution and low-resolution views of normal samples.

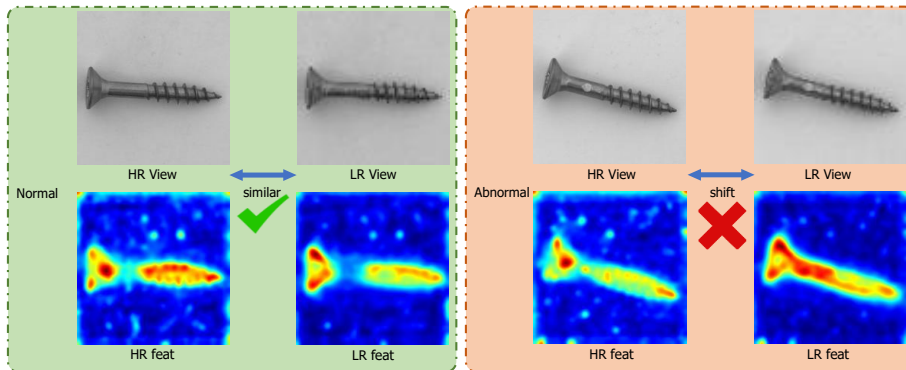


Fig. 1: Visualization of feature responses extracted by a pretrained backbone under different resolutions. Normal samples show consistent activation patterns across high- and low-resolution views, while anomalous samples exhibit pronounced response shifts after resolution reduction due to the degradation of fine-grained structural cues.

Given an input image, dual-resolution features are extracted by a shared frozen backbone and aligned through a learnable guidance module that exploits the asymmetric characteristics of high- and low-resolution representations. High-

resolution features are further decomposed into structure and detail priors, which jointly guide the refinement of low-resolution features via conditional modulation and gated residual correction. During inference, anomalies are detected as regions where cross-resolution alignment breaks down. In addition, a noise-aware data augmentation strategy is introduced to improve robustness against nuisance patterns commonly observed in industrial environments.

The main contributions of this work are summarized as follows:

- We propose an unsupervised anomaly detection framework that identifies anomalies through cross-resolution feature inconsistency.
- We design a structure–detail decoupled guided alignment module that enables stable cross-resolution feature alignment without updating backbone parameters.
- We introduce a noise-aware data augmentation strategy to enhance robustness and reduce false positives in industrial scenarios.

The remainder of this paper is organized as follows. Section 2 reviews related work, Section 3 presents the proposed method, Section 4 reports experimental results, and Section 5 concludes the paper.

2 Related Works

Advancements in industrial anomaly detection have been driven by diverse methodologies focused on identifying defects with minimal labeled data. This section reviews key works in the field, which fall into the following categories.

2.1 Reconstruction-based Anomaly Detection

Reconstruction-based methods identify anomalies by learning to model the distribution of normal data and defect deviations through reconstruction errors. Early generative works, such as SPADE [13], introduced spatially-adaptive normalization for high-fidelity semantic image synthesis, influencing subsequent methods that leverage conditional generation for data augmentation or reconstruction. A notable limitation of standard auto-encoders is their tendency to generalize too well, potentially reconstructing anomalies. To address this, Dong Gong et al. [6] proposed a memory-augmented deep autoencoder (MemAE), which constrains the latent representation by correlating it with a memory bank of prototypical normal patterns, effectively preventing the reconstruction of anomalous regions.

Building on the principle of constrained reconstruction, [20] proposed RIAD (Reconstruction by Inpainting for Visual Anomaly Detection), a novel approach that frames anomaly detection as a self-supervised reconstruction-by-inpainting problem. Unlike standard auto-encoding methods, RIAD randomly removes and reconstructs partial image regions from partial inpainting. By forcing the model to learn from incomplete data, RIAD achieves state-of-the-art results on challenging anomaly detection benchmarks.

Further advancing reconstruction-based paradigms, [9] introduced the Dual-Interrelated Diffusion Model for few-shot anomaly image generation. Their approach tackles the critical challenge of data scarcity in industrial defect detection by using dual-interrelated diffusion processes to generate anomaly images with limited examples. This enables more effective anomaly detection, as the model learns from very few anomaly samples through sophisticated diffusion modeling techniques.

2.2 Feature-based Anomaly Detection

Feature-based methods leverage pre-trained representations and feature matching strategies for anomaly detection. A foundational work in this area is PaDiM (Patch Distribution Modeling) [4]. PaDiM utilizes a pre-trained convolutional neural network to extract patch-level features, models their multivariate Gaussian distributions from normal training images, and detects anomalies by computing the Mahalanobis distance of test patches to the learned normal distribution, achieving robust localization performance. Extending this paradigm, PatchCore [15] focuses on achieving total recall in industrial anomaly detection by constructing a memory bank of nominal patch features and using a nearest-neighbor search for scoring. This approach maximizes detection sensitivity while maintaining precision, addressing the practical requirement of minimizing false negatives in industrial inspection scenarios.

Further advancing this paradigm, UniAD [18] proposed a unified model for multi-class anomaly detection called UniAD. Their approach utilizes a memory bank and prototype learning to achieve robust anomaly discrimination across multiple object categories, demonstrating strong performance by effectively modeling normal feature distributions across diverse classes.

2.3 Zero-shot and Few-shot Anomaly Detection

Recent studies have explored leveraging large-scale vision–language models to perform anomaly detection with little or no task-specific training data. In particular, the emergence of CLIP [14] has inspired a line of work that formulates anomaly detection as a vision–language similarity or alignment problem.

Early efforts such as WinCLIP [8] demonstrate that carefully designed prompts enable effective zero-shot and few-shot anomaly recognition. Building on this idea, AnomalyCLIP [21] introduces anomaly-aware prompt learning to improve pixel-level localization, while CLIP-AD [3] contrasts normal and abnormal semantic embeddings to avoid category-specific training. PromptAD [11] further explores prompt-conditioned feature alignment under few-shot supervision for anomaly segmentation.

Beyond prompt-based formulations, several methods investigate more structured representations to enhance generalization. April-GAN [2] synthesizes diverse anomaly patterns via adversarial generation, whereas MetaUAS [5] adopts a meta-learning paradigm to enable rapid adaptation across categories. MAE-DAY [16] combines masked autoencoding with CLIP to learn robust normal

representations without explicit anomaly supervision. Overall, these approaches highlight the promise of vision–language models in reducing annotation requirements while achieving competitive anomaly detection performance.

3 Method

To overcome the key challenges of modeling anomalies across multiple scales, the limited sensitivity to fine-grained defects in reconstruction-based methods, and the overfitting of normal patterns in unsupervised industrial anomaly detection, this paper proposes an unsupervised anomaly detection framework based on cross-resolution feature alignment with guided representation learning. By exploiting the asymmetric representational characteristics of high- and low-resolution features, to approach explicitly converts cross-resolution inconsistency into a reliable anomaly signal for detection.

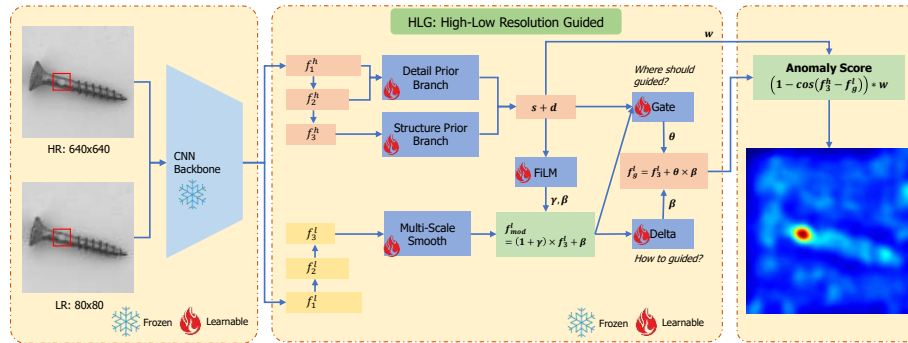


Fig. 2: High-resolution (HR) and low-resolution (LR) images are processed by a shared frozen backbone to extract multi-scale features. The learnable HLGFA module performs structure-guided refinement of low-resolution features using high-resolution representations. Anomalies are detected as regions where cross-resolution feature alignment fails.

3.1 High–Low Resolution Feature Guide

As illustrated in Fig. 2, the proposed framework adopts a dual-resolution feature guidance strategy to leverage the asymmetric representational characteristics of high- and low-resolution (HR and LR) features. High-resolution (HR) representations provide structural and detail priors to guide the refinement of low-resolution (LR) features. This is because HR features preserve richer structural and spatial information, while LR features offer a more compact and noise-tolerant abstraction.

Given an input image x , we construct a high-resolution view x^h and a low-resolution view x^l via down-sampling. Both views are processed by a shared

backbone encoder $B(\cdot)$, producing multi-stage feature representations $\{f_s^h\}$ and $\{f_s^l\}$ at different semantic levels.

Due to the inherent resolution mismatch, LR features are first spatially re-sized to match their HR counterparts:

$$\bar{f}_s^l = \mathcal{U}_s(f_s^l), \quad (1)$$

where $\mathcal{U}_s(\cdot)$ denotes a stage-specific up-sampling operator. This operation ensures spatial correspondence while preserving the compact semantics of LR features.

Rather than directly enforcing feature similarity, which is often unstable under resolution discrepancies, we introduce a learnable guided alignment operator $\mathcal{G}_s(\cdot)$. This operator refines LR features by injecting guidance from HR representations, providing a more effective and adaptive alignment:

$$\hat{f}_s^l = \mathcal{G}_s(\bar{f}_s^l, f_s^h). \quad (2)$$

In practice, HR features serve as guidance signals modulating and correcting LR features. Mean while LR features remain the primary carriers of anomaly-sensitive representations.

During inference time, anomalies are detected as spatial regions where cross-resolution consistency is violated. The anomaly score is computed as:

$$\mathcal{A}(x) = \sum_s \left\| \hat{f}_s^l(x) - f_s^h(x) \right\|_2, \quad (3)$$

where larger discrepancies indicate stronger abnormality. This formulation directly transforms cross-resolution feature inconsistency into a reliable anomaly signal, as visualized in Fig. 2.

3.2 Structure–Detail Decoupled Guidance

A key challenge in cross-resolution feature alignment lies in the entangled nature of high-resolution (HR) representations, where global structure and fine-grained details coexist in the same feature space. Directly using HR features as guidance often leads to unstable supervision, as local noise or repetitive textures may dominate the alignment signal.

To mitigate this issue, we explicitly decompose HR features into two complementary priors: a *structure prior* and a *detail prior*, as illustrated in Fig. 3. The structure prior is extracted from deeper HR features using multi-scale depthwise convolutions to model stable global layouts, while the detail prior is derived from shallower HR features through spatial alignment and lightweight channel projection, retaining informative local cues while suppressing excessive high-frequency noise. The two priors are combined into a unified guidance representation:

$$g_s = s_s + d_s, \quad (4)$$

where s_s and d_s denote the structure and detail priors, respectively.

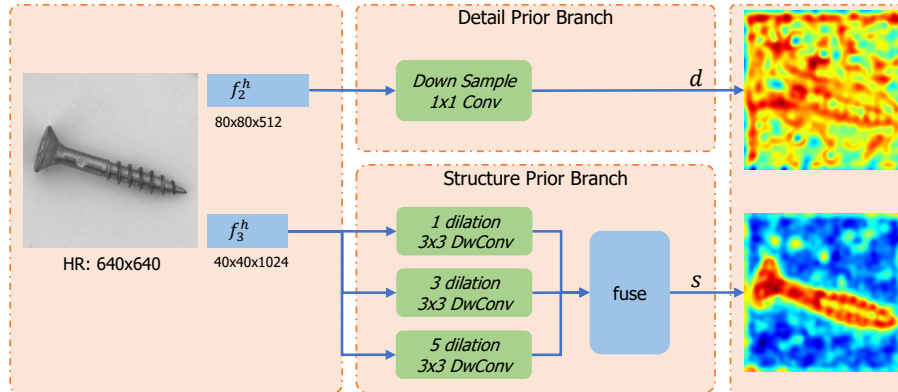


Fig. 3: Illustration of the proposed structure–detail decoupled guidance. High-resolution (HR) features are decomposed into a structure prior and a detail prior. The structure prior captures stable semantic layouts via multi-scale depthwise convolutions, while the detail prior preserves informative local cues through lightweight spatial alignment and channel projection, enabling stable cross-resolution guidance.

As shown in Fig. 2, low-resolution (LR) features are first spatially aligned and stabilized, and then modulated via a FiLM-based transformation conditioned on the structure–detail guidance:

$$\tilde{f}_s^l = \text{FiLM}(f_s^l | g_s), \quad (5)$$

where $\text{FiLM}(\cdot)$ denotes a feature-wise affine modulation conditioned on g_s .

Rather than enforcing strict feature-level consistency, we adopt a lightweight gated residual correction mechanism. The refined LR features are obtained as:

$$\hat{f}_s^l = f_s^l + \mathcal{G}(g_s, \tilde{f}_s^l), \quad (6)$$

where $\mathcal{G}(\cdot)$ denotes a shallow gated residual predictor that adaptively determines *where* and *how* HR guidance should be injected. This formulation avoids overly restrictive pixel-wise constraints and enables flexible, data-driven cross-resolution alignment.

While structure–detail guidance improves cross-resolution alignment during training, we further exploit the stability of the structure prior to estimate spatial reliability during inference, as illustrated in Fig. 4. Intuitively, anomaly responses caused by unreliable or noisy guidance should be suppressed, even if cross-resolution discrepancies are observed.

Specifically, we compute a local structural consistency score based on the normalized guidance representation:

$$\text{sim}(x) = \mathbb{E}_{p \in \mathcal{N}(x)} [\langle \tilde{g}_s(x), \tilde{g}_s(p) \rangle], \quad (7)$$

where $\mathcal{N}(x)$ denotes the local neighborhood of x and $\tilde{g}_s(x) = g_s(x) / \|g_s(x)\|_2$.

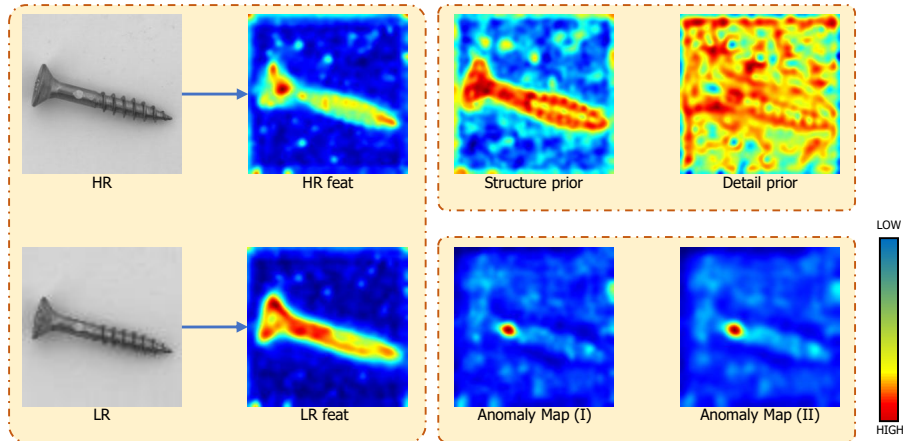


Fig. 4: Visualization of the proposed structure–detail decoupled guidance and structure-based reliability modulation. HR and LR images are encoded into multi-scale features. During inference, anomaly maps derived from cross-resolution discrepancies are further modulated by a structure-based reliability weight, which suppresses spurious responses in structurally unstable regions.

The final reliability-aware anomaly response is obtained by:

$$\mathcal{A}'(x) = \sigma\left(\frac{\text{sim}(x) - \tau}{\delta}\right) \cdot \mathcal{A}(x), \quad (8)$$

where τ and δ control the consistency threshold and transition smoothness, respectively.

3.3 Noise-Aware Data Augmentation

In real-world industrial inspection, normal samples often contain unavoidable nuisance factors such as hairs, stains, or contamination noise. Although visually irrelevant, these patterns can interfere with cross-resolution feature alignment, leading to false positives. As shown in Fig. 5, even defect-free products may exhibit minor surface irregularities that produce strong local activations, causing the model to incorrectly interpret them as anomalies.

To improve robustness, we apply noise-aware data augmentation during training by injecting sparse point noise and structured stripe noise into normal samples, mimicking common contamination patterns. Noise is applied consistently to both HR and LR views, encouraging the model to focus on stable structural semantics rather than local noise, thereby reducing false positive detections.

3.4 Backbone Selection

We empirically observe that ResNet-style backbones, especially Wide-ResNet [19] variants, consistently outperform DenseNet [7] and ConvNeXt [12] architectures

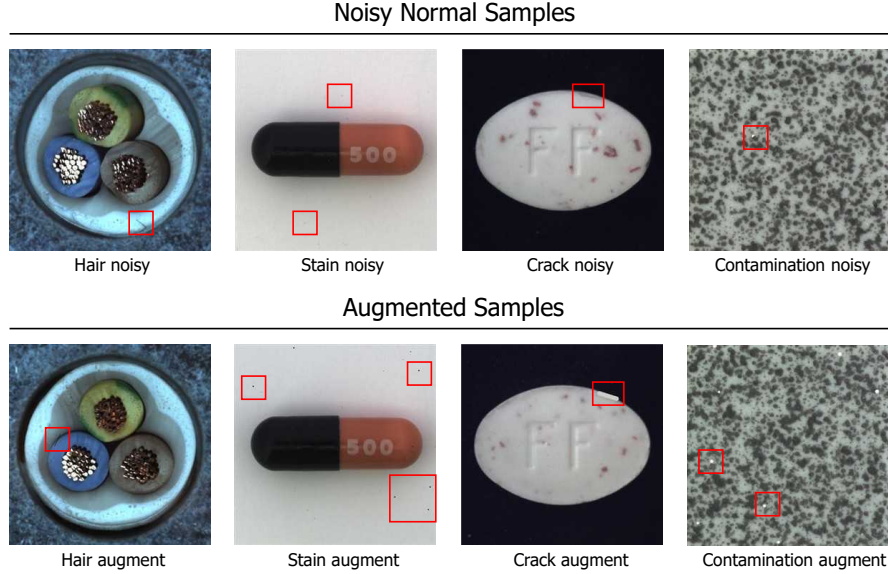


Fig. 5: The top row shows typical nuisance patterns commonly observed in defect-free products, including hairs, stains, cracks, and contamination noise. The bottom row illustrates our noise-aware augmentation strategy, where sparse point noise and structured stripe noise are synthetically injected into normal samples to simulate real-world contamination.

within the proposed framework. This is likely due to the spatially diffused feature propagation enabled by residual connections, which promotes smooth and coherent feature responses across layers.

Such properties are particularly beneficial for cross-resolution alignment, where reliable guidance depends on stable and spatially coherent representations. In contrast, architectures that emphasize aggressive feature reuse or localized depthwise convolutions tend to amplify texture-level noise, which is detrimental to robust anomaly detection, leading to less reliable results.

3.5 Training Objective

All training objectives are computed exclusively on normal samples to ensure the model learns the characteristics of normal data. The core objective enforces cross-resolution feature alignment by minimizing a cosine similarity loss between the high-resolution features f^h and the aligned low-resolution features \hat{f}^l :

$$\mathcal{L}_{\text{align}} = \mathbb{E} \left[1 - \frac{\langle f^h, \hat{f}^l \rangle}{\|f^h\|_2 \|\hat{f}^l\|_2} \right]. \quad (9)$$

This formulation encourages resolution-invariant representations while remaining insensitive to feature magnitude, making it particularly suitable when using a frozen backbone.

To improve robustness under noisy or ambiguous conditions, we further augment the alignment objective with several lightweight auxiliary regularizers. Specifically, we introduce (i) a focal-weighted ℓ_1 feature consistency term to emphasize misaligned regions, (ii) a distribution-level consistency constraint based on Jensen–Shannon divergence by treating channel-wise normalized features as probability distributions, and (iii) a Gram-matrix matching loss to encourage second-order structural consistency between high- and low-resolution features. In addition, a classification-based auxiliary loss is optionally employed to provide weak semantic regularization.

The overall training objective is defined as:

$$\mathcal{L} = \mathcal{L}_{\text{align}} + \lambda_{\ell_1} \mathcal{L}_{\ell_1} + \lambda_{\text{JS}} \mathcal{L}_{\text{JS}} + \lambda_{\text{Gram}} \mathcal{L}_{\text{Gram}} + \lambda_{\text{cls}} \mathcal{L}_{\text{cls}}, \quad (10)$$

where the auxiliary terms mainly serve as stabilizers during training. Unless otherwise specified, $\mathcal{L}_{\text{align}}$ is always enabled, while the remaining terms are assigned modest weights and activated only when necessary.

4 Experiments

4.1 Experimental Setup

We evaluate on **MVTec AD** [1], a standard industrial anomaly detection benchmark with 15 categories of object and texture defects. Following the unsupervised protocol, only normal images are used for training in a category-agnostic manner. We report **pixel-level** metrics (AUC-P, AP-P, F1-P, PRO) and **image-level** metrics (AUC-I, AP-I, F1-I) following the official evaluation protocol.

We use a **frozen** Wide-ResNet-50 backbone pretrained on ImageNet with 640×640 input resolution. Training uses Adam optimizer (learning rate 1×10^{-3} to 1×10^{-4} with cosine annealing) for 100 epochs with batch size 32 on normal samples only. Inference requires no memory bank or reference samples—**anomaly maps** are computed directly from cross-resolution feature inconsistency.

4.2 Overall Comparison with State-of-the-Art Methods

Table 1 presents quantitative comparisons between our method and representative state-of-the-art approaches, including RD4AD [15], AnomalyCLIP [21], CRAD [10], and NAGL [17].

For fair comparison, we report four core metrics: image-level AUROC (AUC-I), pixel-level AUROC (AUC-P), and pixel-level Average Precision (AP-P).

As shown in Table 1, our method achieves the best overall performance across both image-level and pixel-level metrics. In particular, HLGFA consistently outperforms competing methods in pixel-level AP, indicating stronger robustness to background noise and improved suppression of false-positive responses.

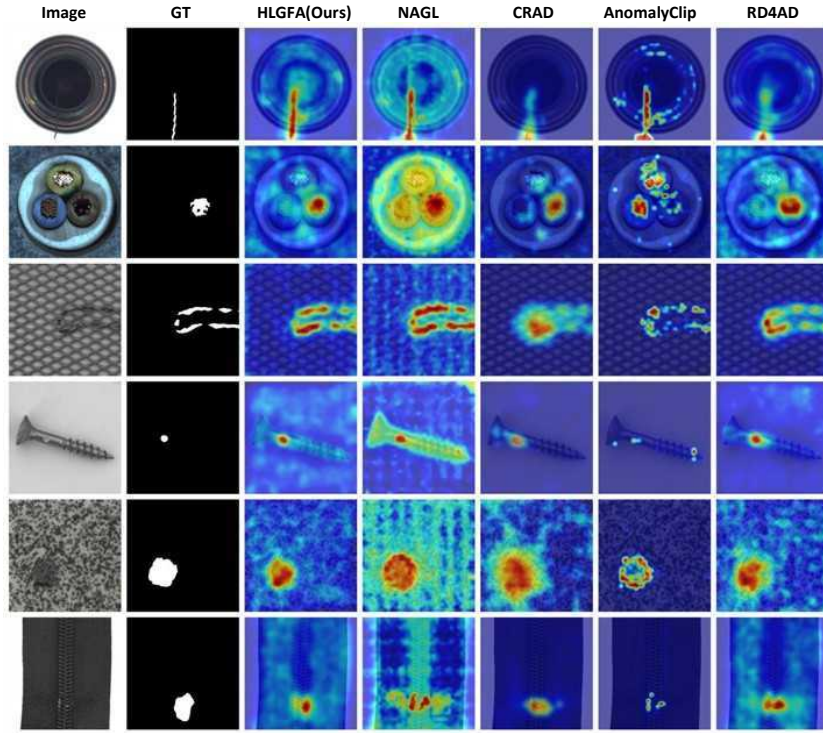


Fig. 6: Qualitative comparison of anomaly localization results on the MVTEC AD dataset. From left to right: input image, ground-truth mask (GT), HLGFA (ours), NAGL, CRAD, AnomalyCLIP, and RD4AD. HLGFA produces more compact and accurate anomaly responses that align better with the ground-truth regions, while suppressing spurious activations on normal areas.

Table 1: Quantitative comparison on MVTEC AD. We report image-level ROC-AUC (ROC-I), pixel-level ROC-AUC (ROC-P), and pixel-level AP (AP-P). Best and second-best results are highlighted in bold and blue, respectively.

Category	RD4AD (CVPR'22)			AnomalyCLIP (ICLR'24)			CRAD (ECCV'24)			NGAL (NeurIPS'25)			HLGFA (Ours)		
	ROC-I	ROC-P	AP-P	ROC-I	ROC-P	AP-P	ROC-I	ROC-P	AP-P	ROC-I	ROC-P	AP-P	ROC-I	ROC-P	AP-P
bottle	99.6	97.7	68.2	88.7	90.4	55.3	99.8	98.3	74.6	99.8	97.1	79.5	99.6	98.7	82.3
cable	79.4	85.4	26.4	70.3	78.9	12.3	97.7	98.1	63.7	91.2	93.5	56.4	95.8	97.9	70.2
capsule	97.5	98.6	43.6	89.5	95.8	27.7	98.0	98.6	43.0	80.8	97.7	39.1	92.5	98.2	47.2
carpet	94.6	98.7	56.2	100.0	98.8	56.6	99.6	98.7	51.0	100.0	99.2	64.9	95.3	99.3	73.7
grid	97.1	99.2	45.0	97.8	97.3	24.1	99.8	98.4	29.2	100.0	99.3	51.9	95.0	99.2	46.0
hazelnut	100.0	98.9	64.1	97.2	97.2	43.4	99.4	98.5	54.8	99.9	99.2	76.1	99.8	99.2	71.4
leather	100.0	99.4	42.0	99.8	98.6	22.8	100.0	99.2	40.6	100.0	99.0	43.4	100.0	99.7	67.2
metal_nut	96.7	93.9	61.8	92.4	74.6	26.5	100.0	96.7	73.1	99.8	94.8	71.6	100.0	97.2	79.9
pill	96.0	98.5	76.6	81.1	91.8	34.1	96.0	97.6	67.8	92.3	92.5	45.9	94.7	94.4	63.3
screw	96.9	99.4	44.1	82.1	97.5	27.5	96.4	99.1	33.6	81.3	98.3	42.7	96.7	98.9	46.6
tile	97.1	95.4	50.6	100.0	94.7	61.7	99.8	93.4	48.8	99.7	93.4	62.7	100.0	97.8	73.5
toothbrush	98.9	99.0	56.0	85.3	91.9	19.3	88.1	98.9	45.7	88.3	99.0	69.6	96.9	99.3	61.5
transistor	92.9	87.9	41.9	93.9	70.8	15.6	99.2	97.2	69.4	85.1	85.1	52.5	99.5	94.3	60.3
wood	99.1	96.0	52.9	96.9	96.4	52.7	99.6	94.4	44.1	100.0	95.9	68.2	97.7	96.1	64.4
zipper	35.2	96.1	21.9	98.4	91.3	38.7	98.9	97.6	49.2	98.7	97.9	57.1	99.3	98.4	67.7
Average	92.1	96.3	50.1	91.6	91.1	34.5	98.2	97.7	52.6	94.5	96.1	58.8	97.5	97.9	65.0

These quantitative advantages are further supported by the qualitative results in Fig. 6, where HLGFA produces more compact and accurate anomaly maps that better align with the ground-truth defect regions, while avoiding spurious activations on normal structures.

Notably, our approach achieves competitive or superior localization accuracy without relying on reconstruction, diffusion sampling, or memory banks during inference.

4.3 Ablation Study on Feature Alignment Loss

To investigate the contribution of different terms in the proposed feature alignment loss, we conduct a series of ablation experiments on the MVTec AD dataset by progressively enabling individual loss components. All variants are trained under identical settings, and the only difference lies in the composition of the feature alignment loss. For all ablation experiments, Wide-ResNet50 [19] is utilized as the fixed backbone network.

Specifically, we evaluate the following loss configurations:

- **Cosine**: cosine similarity only.
- **Cosine + JS**: cosine similarity with Jensen–Shannon divergence (0.1).
- **Cosine + Gram**: cosine similarity with Gram matrix loss (0.5).
- **Cosine + L1**: cosine similarity with ℓ_1 loss (0.5).
- **Full**: cosine similarity with ℓ_1 (0.5), Jensen–Shannon (0.5), and Gram losses (0.5).

This ablation setting allows us to isolate the effect of each auxiliary loss term and to analyze how different forms of feature-level regularization contribute to cross-resolution alignment and anomaly localization performance.

Table 2: Ablation study on the composition of the feature alignment loss on the MVTec AD dataset. All models use Wide-ResNet50 as the backbone.

Cos	JS	Gram	L1	AUROC-I \uparrow	AP-I \uparrow	AUROC-P \uparrow	AP-P \uparrow	PRO-P \uparrow
✓				94.2	98.2	97.7	61.1	88.6
✓	✓			92.7	97.0	97.8	58.4	87.9
✓		✓		94.8	98.2	97.8	62.5	89.0
✓			✓	97.2	99.0	97.7	65.0	89.9
✓	✓	✓	✓	97.5	99.2	97.9	65.0	91.7

As reported in Table 2, cosine similarity alone provides a strong baseline but limited localization capability, reflected by lower pixel-level AP and PRO scores. Interestingly, directly adding Jensen–Shannon (JS) divergence causes slight performance degradation, as it enforces global distributional consistency that may over-regularize alignment and suppress subtle discrepancies crucial for anomaly

detection. In contrast, Gram matrix loss consistently improves pixel-level metrics by capturing higher-order feature correlations, while ℓ_1 loss contributes the most significant gain by enforcing element-wise consistency and stabilizing cross-resolution correspondence.

Finally, combining all loss components yields the best overall performance. The full objective benefits from complementary regularization: cosine similarity preserves directional alignment, ℓ_1 enforces local correspondence, Gram loss captures global statistics, and JS divergence provides mild distributional smoothing, resulting in superior localization accuracy and robustness.

4.4 Per-Category Analysis of Our Method

Table 3: Per-category quantitative results on MVTec AD. AUC-P, AP-P, F1-P, and PRO are pixel-level metrics, while AP-I, AUC-I, and F1-I denote image-level performance.

	Category	AUC-I	AP-I	F1-I	AUC-P	AP-P	PRO-P	F1-P
Textures	carpet	95.3	98.6	93.7	99.3	73.7	93.9	68.9
	grid	95.0	98.3	93.0	99.2	46.0	87.8	47.5
	leather	100.0	100.0	100.0	99.7	67.2	96.7	63.3
	tile	100.0	100.0	99.4	97.8	73.5	90.7	71.8
	wood	97.7	99.3	96.8	96.1	64.4	88.1	59.3
Objects	bottle	99.6	99.9	99.2	98.7	82.3	94.7	76.3
	cable	95.8	97.7	91.1	97.9	70.2	92.9	67.0
	capsule	92.5	98.3	94.3	98.2	47.2	92.9	48.5
	hazelnut	99.8	99.9	98.6	99.2	71.4	94.8	71.0
	metal_nut	100.0	100.0	100.0	97.2	79.9	89.4	80.8
	pill	94.7	99.1	94.7	94.4	63.3	88.3	63.4
	screw	96.7	98.8	95.7	98.9	46.6	92.7	49.0
	toothbrush	96.9	98.8	95.1	99.3	61.5	91.6	66.7
	transistor	99.5	99.3	97.5	94.3	60.3	89.5	60.1
zipper	99.3	99.8	98.7	98.4	67.7	92.0	65.6	
	Average	97.5	99.2	96.5	97.9	65.0	91.7	63.9

To provide a detailed performance profile of the proposed approach, Table 3 reports the complete per-category results of our method on MVTec AD, including pixel-level (AUC-P, AP-P, F1-P, PRO) and image-level (AUC-I, AP-I, F1-I) metrics.

The results demonstrate that HLGFA achieves consistently high image-level detection accuracy, with an average AP-I of 99.2%, while maintaining strong pixel-level localization performance across both texture and object categories.

In challenging categories such as *grid*, *capsule*, and *screw*, where regular textures and small defects often cause severe false alarms, our method still maintains stable AP-P and PRO scores, highlighting the effectiveness of structure–detail guided alignment.

5 Conclusion

In this paper, we proposed **HLGFA**, a novel unsupervised anomaly detection framework based on *cross-resolution guided feature alignment*. Unlike reconstruction- or memory-based methods that explicitly model normal appearance, HLGFA exploits the inherent asymmetry between high- and low-resolution representations and converts their alignment inconsistency into reliable anomaly signals.

The key insight of HLGFA is that high-resolution features preserve stable structural semantics, whereas low-resolution features tend to over-generalize toward normal patterns. By introducing a structure–detail decoupled guidance mechanism, HLGFA refines low-resolution representations under high-resolution supervision, enhancing sensitivity to subtle anomalies while maintaining localization accuracy. Consequently, anomalies are revealed as regions where cross-resolution alignment breaks down, rather than being inferred from potentially unreliable reconstruction errors.

Extensive experiments on MVTec AD validate the effectiveness of HLGFA, demonstrating consistently strong performance at both image and pixel levels, with particularly notable gains in pixel-wise localization metrics such as AU-ROC, PRO, and F1-score. Ablation studies further confirm the complementary contributions of the structure prior, detail prior, and noise-aware data augmentation.

From an industrial perspective, HLGFA is well suited for real-world AOI applications: it requires only normal samples for training, leverages pretrained backbones without task-specific fine-tuning, and produces stable, interpretable anomaly maps based on feature inconsistency. These properties make HLGFA especially practical for industrial scenarios characterized by diverse defects and scarce abnormal data.

In future work, we will explore extending cross-resolution alignment to multi-modal inputs and foundation models, as well as adaptive consistency modeling to further enhance robustness and anomaly confidence estimation.

References

1. Bergmann, P., Fauser, M., Sattlegger, D., Steger, C.: Mvtec ad — a comprehensive real-world dataset for unsupervised anomaly detection. In: 2019 IEEE/CVF Conference on Computer Vision and Pattern Recognition (CVPR). pp. 9584–9592 (2019). <https://doi.org/10.1109/CVPR.2019.00982>
2. Chen, X., Han, Y., Zhang, J.: April-gan: A zero-/few-shot anomaly classification and segmentation method for cvpr 2023 vand workshop challenge tracks 1&2: 1st place on zero-shot ad and 4th place on few-shot ad (2023), <https://arxiv.org/abs/2305.17382>
3. Chen, X., Zhang, J., Tian, G., He, H., Zhang, W., Wang, Y., Wang, C., Liu, Y.: Clip-ad: A language-guided staged dual-path model for zero-shot anomaly detection (2024), <https://arxiv.org/abs/2311.00453>
4. Defard, T., Setkov, A., Loesch, A., Audigier, R.: Padim: a patch distribution modeling framework for anomaly detection and localization (2020), <https://arxiv.org/abs/2011.08785>
5. Gao, B.B.: Metauas: Universal anomaly segmentation with one-prompt meta-learning (2025), <https://arxiv.org/abs/2505.09265>
6. Gong, D., Liu, L., Le, V., Saha, B., Mansour, M.R., Venkatesh, S., van den Hengel, A.: Memorizing normality to detect anomaly: Memory-augmented deep autoencoder for unsupervised anomaly detection (2019), <https://arxiv.org/abs/1904.02639>
7. Huang, G., Liu, Z., Weinberger, K.Q.: Densely connected convolutional networks. CoRR **abs/1608.06993** (2016), <http://arxiv.org/abs/1608.06993>
8. Jeong, J., Zou, Y., Kim, T., Zhang, D., Ravichandran, A., Dabeer, O.: Winclip: Zero-/few-shot anomaly classification and segmentation (2023), <https://arxiv.org/abs/2303.14814>
9. Jin, Y., Peng, J., He, Q., Hu, T., Wu, J., Chen, H., Wang, H., Zhu, W., Chi, M., Liu, J., Wang, Y.: Dual-interrelated diffusion model for few-shot anomaly image generation (2025), <https://arxiv.org/abs/2408.13509>
10. Lee, J.C., Kim, T., Park, E., Woo, S.S., Ko, J.H.: Continuous memory representation for anomaly detection (2024), <https://arxiv.org/abs/2402.18293>
11. Li, X., Zhang, Z., Tan, X., Chen, C., Qu, Y., Xie, Y., Ma, L.: Promptad: Learning prompts with only normal samples for few-shot anomaly detection (2024), <https://arxiv.org/abs/2404.05231>
12. Liu, Z., Mao, H., Wu, C.Y., Feichtenhofer, C., Darrell, T., Xie, S.: A convnet for the 2020s (2022), <https://arxiv.org/abs/2201.03545>
13. Park, T., Liu, M.Y., Wang, T.C., Zhu, J.Y.: Semantic image synthesis with spatially-adaptive normalization (2019), <https://arxiv.org/abs/1903.07291>
14. Radford, A., Kim, J.W., Hallacy, C., Ramesh, A., Goh, G., Agarwal, S., Sastry, G., Askell, A., Mishkin, P., Clark, J., Krueger, G., Sutskever, I.: Learning transferable visual models from natural language supervision (2021), <https://arxiv.org/abs/2103.00020>
15. Roth, K., Pemula, L., Zepeda, J., Schölkopf, B., Brox, T., Gehler, P.V.: Towards total recall in industrial anomaly detection. CoRR **abs/2106.08265** (2021), <https://arxiv.org/abs/2106.08265>
16. Schwartz, E., Arbelle, A., Karlinsky, L., Harary, S., Scheidegger, F., Doveh, S., Giryes, R.: Maeday: Mae for few and zero shot anomaly-detection (2024), <https://arxiv.org/abs/2211.14307>

17. Wang, Y., Wang, X., Gong, Y., Xiao, J.: Normal-abnormal guided generalist anomaly detection (2025), <https://arxiv.org/abs/2510.00495>
18. You, Z., Cui, L., Shen, Y., Yang, K., Lu, X., Zheng, Y., Le, X.: A unified model for multi-class anomaly detection (2022), <https://arxiv.org/abs/2206.03687>
19. Zagoruyko, S., Komodakis, N.: Wide residual networks. CoRR **abs/1605.07146** (2016), <http://arxiv.org/abs/1605.07146>
20. Zavrtnik, V., Kristan, M., Skočaj, D.: Reconstruction by inpainting for visual anomaly detection. Pattern Recognition **112**, 107706 (2021). <https://doi.org/10.1016/j.patcog.2020.107706>
21. Zhou, Q., Pang, G., Tian, Y., He, S., Chen, J.: Anomalyclip: Object-agnostic prompt learning for zero-shot anomaly detection (2023), <https://arxiv.org/abs/2310.18961>